

Unconventional mechanical and thermal behaviors of MOF CALF-20

Dong Fan, Supriyo Naskar, Guillaume Maurin*

ICGM, Univ. Montpellier, CNRS, ENSCM, Montpellier, 34095, France

*Corresponding author: guillaume.maurin1@umontpellier.fr

CALF-20 was recently identified as a novel benchmark sorbent for CO₂ capture at the industrial scale, however comprehensive atomistic insight into its mechanical/thermal properties under working conditions is still lacking. In this study, we developed a general-purpose machine-learned potential (MLP) for the CALF-20 MOF framework that predicts the thermodynamic and mechanical properties of the structure at finite temperatures within first-principles accuracy. Interestingly, CALF-20 was demonstrated to exhibit both negative area compression and negative thermal expansion. Most strikingly, upon application of the tensile strain along the [001] direction, CALF-20 was shown to display a distinct *two-step* elastic deformation behavior, unlike typical MOFs that undergo plastic deformation after elasticity. Furthermore, this MOF was shown to exhibit a spectacular fracture strain of up to 27% along the [001] direction at room temperature comparable to that of MOF glasses. These abnormal thermal and mechanical properties make CALF-20 as attractive material for flexible and stretchable electronics and sensors.

Introduction

The flexible Metal-Organic Frameworks (MOFs) also called soft porous crystals or dynamic MOFs have emerged as a smart subclass of MOFs owing to their unprecedented physical properties that challenge conventional conceptions of framework rigidity/fragility in material science.¹⁻⁴ In particular the intriguing mechanical and thermal properties of this family of materials serve as an important cornerstone in expanding their potential application domains.^{2,3,5,6} Notably, some of the flexible MOFs, possess counterintuitive mechanical properties, including negative linear compressibility (NLC),⁷ negative area compressibility (NAC), stretch densification,⁸ and push/pull-twisted among others.⁹ These abnormal pressure-responsive behavior defies the well-known "*compression-contraction*" effect and opens new avenues in many applications, e.g. optoelectronic devices,¹⁰ pressure sensors and intelligent body armor.^{8,11} In addition, some of these materials also exhibit negative thermal expansion (NTE) behavior, which refers to the phenomenon where a material contracts rather than expands upon heating, of potential importance for further development in the field of thermal expansion compensator.

Recently, a $\text{Zn}_2(1,2,4\text{-triazolate})_2(\text{oxalate})$ framework named as CALF-20, was proposed as a novel benchmark sorbent for CO_2 capture combining excellent CO_2/N_2 separation performance in flue gas condition, high hydrolytic stability and easy scalable that made it promotable at the industrial scale.¹² Other CALF-20 derivatives as well as their composites have been equally explored.¹³⁻¹⁷ The structure of this MOF consists of 2D layers of 1,2,4-triazolate-bridged zinc ions pillared by oxalate linkers, forming a three-dimensional (3D) framework.¹² The pillars of the oxalate linker acting as hinges, are connected by zinc triazolate grids parallel to the *ac* plane, offering potentially high flexibility to the 3D framework that might pave the way towards intriguing physical properties (Fig. 1a). However, so far, the mechanical/thermal behaviors of this MOF have been completely overlooked. Beyond a fundamental interest, the lack of understanding on the pressure/thermal-induced structure change of CALF-20 is critical

in the context of using this MOF under diverse operating conditions. The determination of MOF mechanical/thermal properties generally requires the deployment of high-tech and specialized equipment as well as high-quality samples making the whole testing process far to be trivial.^{18,19} Meanwhile, *in-silico* simulation approaches offer promising alternatives to not only accurately predict but also gain atomistic insight and even rationalize the MOF structure behaviors upon diverse environments.^{20–22} Herein, the unprecedented computational exploration of the physical properties of the emblematic CALF-20 MOF calls for the development and application of cost-effective and accurate molecular simulation tools and the expected outcomes might reveal new phenomena paving the way towards novel prospective for this MOF.

In this context, the mechanical and thermal behaviors of CALF-20 was explored in-depth by combining extensive Density Functional Theory (DFT) calculations and high-precision machine-learning potential molecular dynamics (MLP-MD) simulations. CALF-20 was demonstrated to exhibit anomalous structural response to both temperature and pressure stimuli, resulting in the coexistence of NAC and NTE effects. This makes this material highly attractive for mechanical/thermal sensing, besides its actual application in the field of CO₂ capture. Decisively our simulations revealed that CALF-20 exhibits an abnormal strain-softening at both 0K and room temperature under uniaxial tensile strain that eventually leads to the formation of a new metastable structure. From a methodology perspective, the MLP-MD approach was demonstrated to be a powerful tool for anticipating unconventional structural features of CALF-20 upon stimuli at finite temperature.

Results

Negative area compressibility behavior. DFT calculations were first performed at 0K to determine the elastic properties of CALF-20 via a comprehensive tensorial analysis based on a finite difference approach,²³ as implemented in the VASP code.²⁴ These calculations evidenced that CALF-20 exhibits a large anisotropy in its linear

compressibility, with a positive contribution along the *c* axis (170 TPa⁻¹) (see Fig. 1b), while both *a* and *b* axis show a negative contribution (maximum of -24 and -32 TPa⁻¹ respectively, see Supplementary Fig. S1). This unusual mechanical response of the MOF framework corresponds to a rather rare NAC behavior. This implies that as the MOF is compressed, the *ab*-plane expands spontaneously to maintain the minimum energy principle of the system, while the *c*-axis shrinks. These calculations revealed that the predicted Young's modulus (Fig. 1b) and Poisson's ratio (Fig. 1c) are also highly anisotropic, with both maxima observed quasi along the *a*-axis (Supplementary Fig. S2) corresponding to the direction of the pillared oxalate ligands, allowing a stronger resilience of the MOF framework, whereas the *bc* plane corresponds to the more flexible rhombic-shaped zinc triazolate grid. It is worth noting that the [100] and [010] directions are the principal axes of the rhombic shaped zinc triazolate grid, therefore, when *b*-axis is elongated (compressed), the zinc triazolate layer is deformed by reducing (stretching) the length of all the connectors along the *c*-axis to minimize the energy of the overall system. Therefore, the unique flexible behavior of CALF-20 originates from its topology: Each oxalate ligand utilizes its tetradentate oxygen atoms to vertically stretch two independent zinc triazolate ligand forming a crossed 3D configuration with zinc triazolate grids and oxalate pillars.

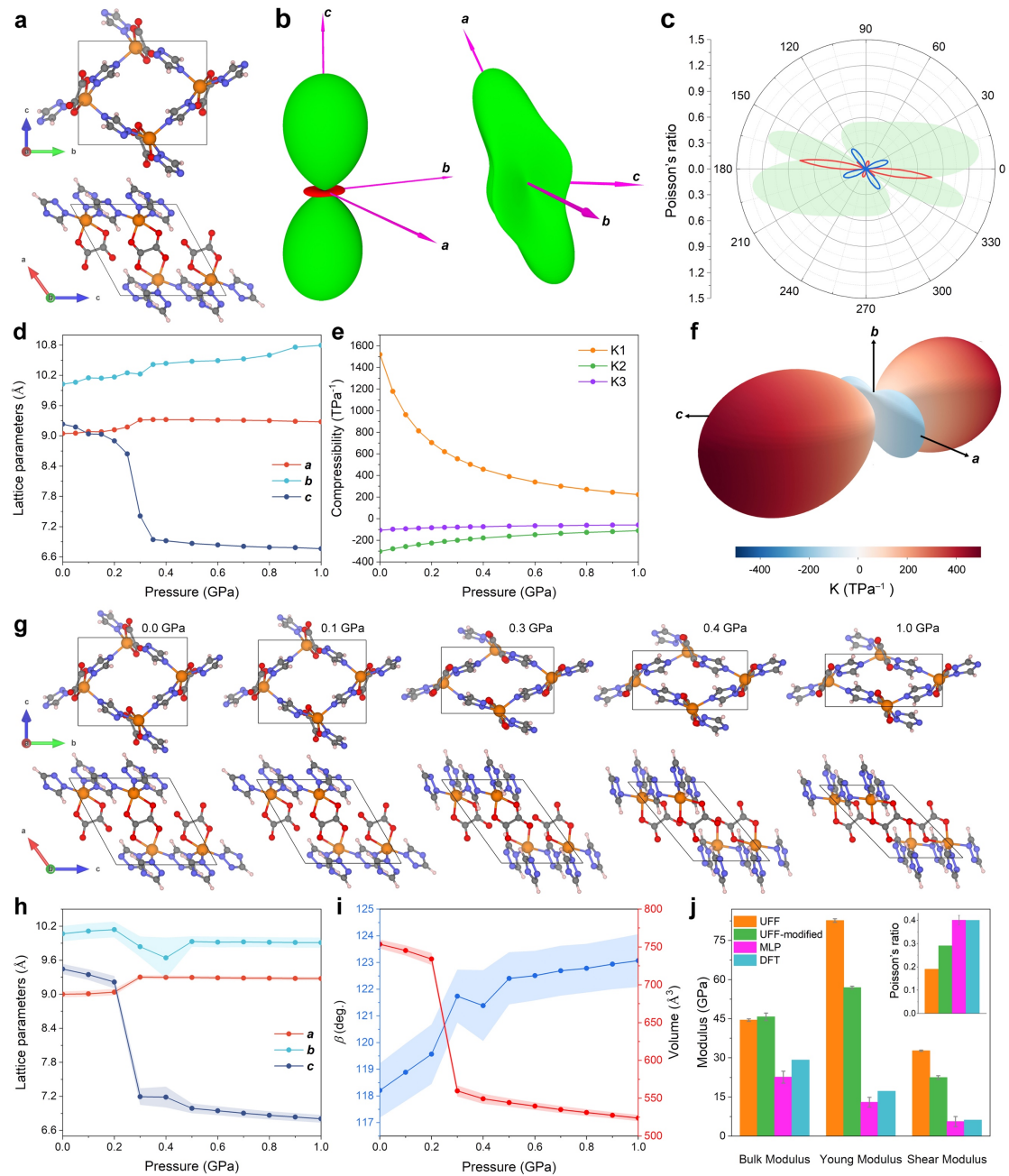


Fig. 1 | Anisotropic mechanical properties of CALF-20 predicted by DFT and finite temperature NPT MLP-MD simulations. (a) DFT-optimized structure of CALF-20 viewed along different perspectives. (b) Three dimensional representations of the linear compressibility (left) and Young's modulus (right). Positive and negative values for linear compressibility are indicated as green and red respectively. (c) The elastic constant derived from the spatial dependence of the Poisson's ratio in ac plane. Positive and negative contributions are indicated in blue and red lines respectively. Green shadow represents the maximum positive value for Poisson's ratio. (d) Unit-cell parameters changes and corresponding (e) compressibility changes during hydrostatic

compression of CALF-20. (f) 3D mapping of the linear compressibility (TPa^{-1}) derived using the structural parameters under different mechanical pressures as determined by an empirical potential fitting approach.²⁵ (g) Structural evolution of the CALF-20 unit-cell computed by DFT at different pressures. (h, i) Structural parameters and unit-cell volume changes with applied mechanical pressure computed by MLP-MD simulations runs in the NPT ensemble at room temperature (298.15 K). The error bars represent the statistical deviation obtained from the collected 10,000 trajectories. (j) Overall elastic properties simulated by MD calculations using different force fields including MLP as well as UFF and UFF-modified referring to an adjusted UFF parameterization reported in our previous work.¹⁷ and compared to DFT calculations at 0K.

Besides the stiffness tensor-based analysis, the impact of applying a mechanical pressure on the structure was equally examined. Compressibility of material is typically denoted as the relative rate of changes in dimensions with pressure at a fixed temperature, $\kappa = -\frac{1}{v} \left(\frac{\partial v}{\partial P} \right)_T$, where i can be assigned as volume, area, or linear compressibility, respectively.⁸ The compressibility coefficients of the principal axes can be determined within the pressure range.²⁶ Figs. 1d-1e show that the most striking giant NAC phenomenon along \mathbf{a} and \mathbf{b} axis continues monotonically up to 0.3 GPa. The NAC behavior is much more marked along the \mathbf{a} -axis with -188.77 TPa^{-1} strain tensor eigenvector compared to that along the \mathbf{b} -axis (-75.52 TPa^{-1}). The highest positive linear compressibility (PLC) is observed along the direction perpendicular to the \mathbf{ab} plane with a corresponding eigenvector of 501.53 TPa^{-1} , which leads to a substantial compression of the oxalate pillars under pressure (cf. Fig. 1f, Supplementary Table S1). Remarkably, in contrast to other conventional uniaxial NLC materials, CALF20 exhibits a biaxial (or in-plane) NLC behavior, and its compressibility is higher than that of the most extreme existing NLC inorganic materials including $\text{Ag}_3[\text{Co}(\text{CN})_6]\text{-I}$ ($K_c = -76 \text{ TPa}^{-1}$)²⁵ and $[\text{Ag}(\text{en})]\text{NO}_3\text{-I}$ ($K_c = -28.4 \text{ TPa}^{-1}$),²⁷ as well as the most representative flexible MIL-53 MOF material ($K_b = -27 \text{ TPa}^{-1}$).²⁸ The CALF-20 structures simulated upon different applied mechanical pressure are illustrated in Fig. 1g. It is evident that as the pressure increases, the \mathbf{c} -axis shrinks significantly, eventually leading to a decrease in unit cell volume derived from the larger PLC along

the axis. Notably, the applied pressure up to 1 GPa does not induce any structure collapse. Therefore, besides its previously-demonstrated promise as CO₂ sorbent at the industrial level, CALF-20 owing to its unconventional mechanical properties, is predicted to be attractive in pressure-sensitive devices, shock-absorbing materials, artificial muscles, and shape-memory applications among others. Supplementary Figs. S3-S4 that reports the pressure-induced evolution of the CALF-20 lattice parameters further demonstrates that above 1 GPa, a metastable high-pressure phase for CALF-20 exists. Supplementary Fig. S4 shows that such phase is non porous and is associated with a very high density (3.58 g cm⁻³). This novel phase is also demonstrated to remain stable even after releasing the pressure stimulus.

We then developed a MLP-MD strategy (Supplementary Note1 and Figs. S5-S14 for details) to explore the pressure-driven structural flexibility of CALF-20 at room temperature, which is almost unfeasible within the DFT formalism. For all MLP-MD simulations, the $2 \times 2 \times 2$ supercell was used and the structural parameters were finally collected from the last 500 picosecond (ps) (1 nanosecond [ns] in total with 0.5 femtosecond [fs] time steps). Figs. 1h-1i report the MLP-MD derived evolution of the CALF-20 lattice parameters at room temperature upon different applied pressure. These simulations evidenced that both *a*- and *b*-axis dimensions decrease with increasing pressure below 0.30 GPa range in line with the NAC phenomenon revealed above by DFT calculations at 0K. An apparent phase transition is equally observed at 0.30 GPa (Fig. 1d). Moreover, when pressure exceeds 0.50 GPa, *a*- and *b*-axis dimensions remain almost unchanged upon pressure increase, while the *c*-axis dimension decreases linearly (Fig. 1h). This later prediction slightly deviates from the DFT predictions at 0K. Indeed at room temperature, CALF-20 is expected to display a tiny NAC behavior above 0.50 GPa, where the structure evolves as a rigid backbone. The reliability of MLP vs generic UFF force field to describe the mechanical properties of CALF-20 was further assessed using DFT results as benchmark data. Fig. 1i and Supplementary Table S2 evidence that UFF force field leads to a substantial overestimation of both bulk modulus and Young's modulus while it significantly underestimates the shear modulus

by a factor of 3 and 4 respectively compared to the corresponding DFT value. Remarkably, the use of MLP enables to reproduce well the DFT values, especially for the Young's modulus and shear modulus. This comparison emphasizes the reliability of the MLP-MD approach to accurately probe the flexible behavior of CALF-20 at finite temperature at a computational cost far below that of DFT calculations (Supplementary Note2).

Negative thermal expansion behavior. The temperature-dependent thermal properties of CALF-20 were first assessed using the quasi-harmonic approximation (QHA) approach,²⁹ where the influence of temperature is considered through the volume response of the vibrational frequency via the use of phonon anharmonicity.³⁰ Note that conventional QHA approach based on DFT calculations requires the determination of the phonon spectrum under several independent volume deformation of the structure, which requires huge computing resources. The implementation of MLP in the QHA scheme enables a much faster assessment of the corresponding data reported in Fig. 2a (see Supplementary Figs. S15-S16 for details). CALF-20 is thus predicted to exhibit a NTE behavior at low temperature, the lowest NTE value of $-10.56 \times 10^{-6} \text{ K}^{-1}$ at 40K being within the same range than that reported for typical NTE MOFs.^{6,31,32} Notably, a nearly negligible unit cell volume change *versus* temperature is obtained, indicating that as the temperature increases, the lattice shrinks in different orientations to ensure an energy equilibrium, confirming a relatively high flexibility of the CALF-20 framework. Since QHA does not explicitly include anharmonicity³³, its reliability is almost exclusively limited to the low temperature domain. One possibility to extend the applicability of QHA to higher temperature is to carry out AIMD simulations, however, this is extremely time-consuming. Herein, we privileged the implementation of our newly derived MLP validated above on the mechanical properties of CALF-20 to run MLP-MD simulations in the *NPT* ensemble at 1bar and room temperature (298.15 K) with a total simulation time of 1 ns with the use of 0.5 fs time steps to determine the equilibrium lattice parameters of CALF-20, as shown in Figs. 2b-2c. We evidenced that the *b*-axis dimension decreases linearly as the temperature increases, while the overall

unit-cell volume remains almost unchanged, which is in excellent agreement with the prediction based on the QHA approach. Fig. 3c delivers a 3D-representation of the contribution to thermal expansion along each axis (also see Supplementary Table S3). The blue region refers to the NTE behavior domain with negative linear thermal expansion ranging from -4.22 MK^{-1} and -60.81 MK^{-1} . This coefficient is comparable to that exhibited by MOF DUT-60 (-65.0 MK^{-1})³⁴ while it is higher than most other NTE MOFs, *e.g.* Ag(mim) (-24.5 MK^{-1})³⁵ and DUT-49 (-32.778 MK^{-1})³⁶. This suggests that CALF-20 offers promise for applications in the fields of ultrasensitive temperature sensing.

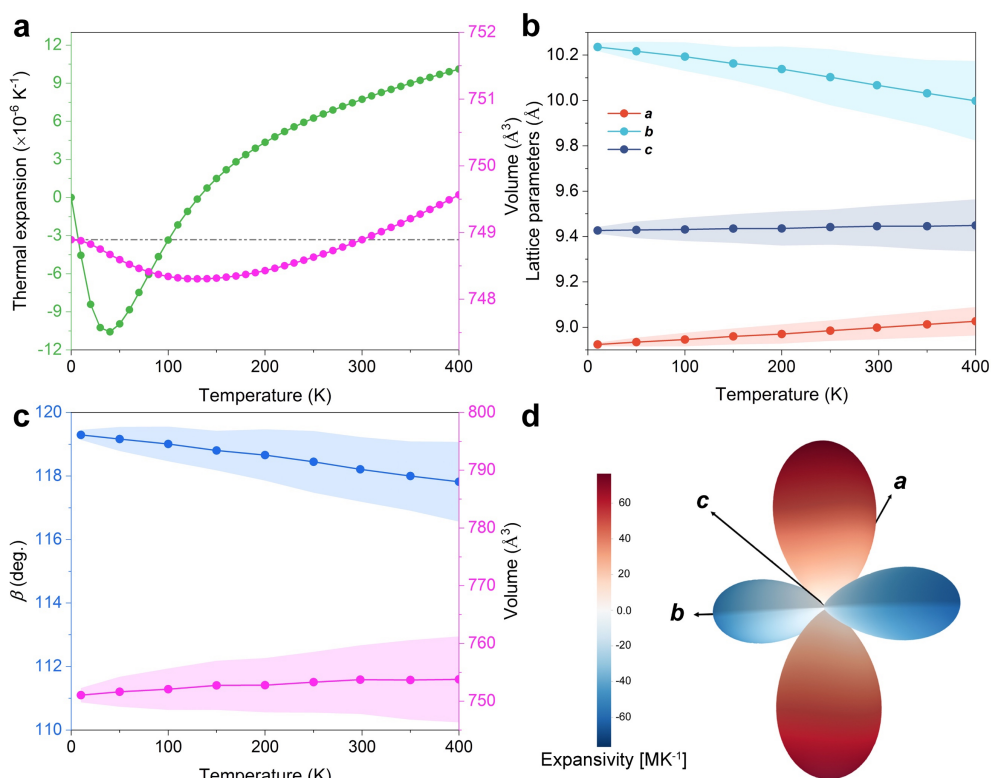


Fig. 2 | Anisotropic Negative Thermal Expansion of CALF-20 revealed by finite temperature NPT MLP-MD simulations. (a) Thermal expansion coefficient and volume change calculated at different temperatures using the quasi-harmonic approximation. (b, c) Equilibrium lattice parameters calculated at various temperatures based on MLP-MD simulations. The error bars indicate the statistical deviation from the collected trajectories. (d) Illustration of the 3D expansivity (MK^{-1}) derived from the empirical potential fitting method using MLP-MD outputs.

Abnormal tension strain response. Typically, a material with *multiple negative phenomena*, e.g. NLC combined with NTE exhibits other peculiar strain-stress behaviors.^{37,38} We therefore examined the deformation behavior of CALF-20 upon the application of ideal tensile strain. The strain-stress curve was first simulated at 0K by DFT calculations (Fig. 3a). The three directions show anisotropic changes, among which the [100] and [010] directions show rapid strain-stiffening after a short elastic deformation.^{39,40} As a result, the [100] and [010] growth directions are predicted to be relatively brittle with failure strains lower than 11% and 22% respectively. However, two independent elastic deformation regions were found with the tensile strain along [001] direction, namely before and after strain-softening to MOF fracture respectively. The first peak at 18.43% strain is associated with a structural transition, *i.e.* strain-softening point, while the second one at 40.25% corresponds to MOF fracture. The rapid change in the stress-strain curve suggest a phase transition. Therefore, the structure near the strain-softening point was considered to calculate the phonon spectrum. Figs. 3b-3c and Supplementary Figs. S17-S19, reveal that there is not any imaginary frequency in the entire Brillouin zone and this confirms the dynamic stability of CALF-20 during the deformation process. In the meantime, we demonstrated that this MOF maintains its structure integrity at very high strain level up to 36.13% (Supplementary Fig. S20). This behavior significantly differs with that exhibited by most of MOF crystals like Ni-TCPP⁴¹ and ZIF-8⁴² etc, that all undergo a fracture above 30% strain.

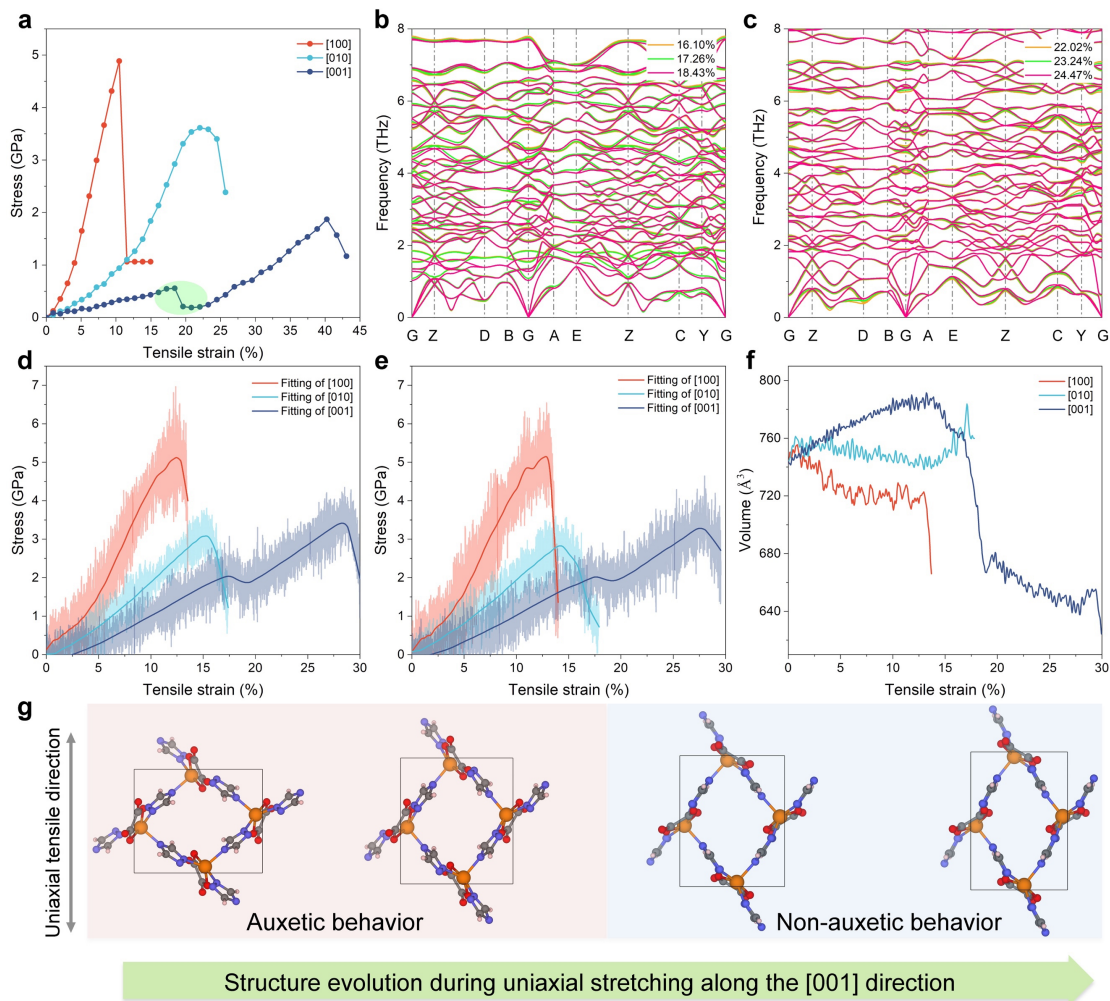


Fig. 3 | Unconventional strain-stress behavior determined by DFT and finite temperature NPT MLP-MD simulations. (a) Tensile strain-stress response along the three directions from DFT calculations at 0K. The green circle indicates the strain-softening region. (b, c) Phonon dispersion spectrum under tensile strain (around the strain-softening range) along the [001] direction calculated based on MLP. Only below 8 THz curves are displayed for clarity. Stress-strain curves at (d) 200 K and (e) 298.15 K derived from MLP-MD simulations. (f) MLP-MD derived volume changes of the CALF-20 at 298.15 K during the application of tensile strain along the three directions. (g) Schematic illustration of the CALF-20 structural evolution upon tensile strain applied along the [001] direction.

MLP-MD calculations were further deployed to explore the temperature effect on the strain-stress behavior of CALF-20. Figs. 3d-3e show the MOF structure response upon the application of the tensile strain along the three directions at 200 K and 298.15

K respectively. These MLP-MD simulations reproduce very well the trend obtained by DFT calculations at 0K while UFF dramatically fails (see Supplementary Figs. S21-S23 for details). In particular, MLP-MD predicts specific stress very close to the DFT-simulated value. These calculations further revealed that the failure strain of CALF-20 remains as high as 27% even at room temperature. To our knowledge, no MOF crystal has ever demonstrated such a wide range of elastic deformation behavior at finite temperature, and the failure is comparable to that of MOF glasses (20%~35% fracture strain recently reported for α -ZIF-62).^{43,44} On the other hand, we found that the temperature effect on the fracture strain of CALF-20 is very small, *e.g.*, the fracture strain along the [100] direction is almost unchanged when the temperature increases from 200 K to room temperature, and the [010] and [001] direction dimensions are reduced by only 1%. This trend is likely to be due to the coexistence of the inherent NTE and NAC behaviors of CALF-20 that makes its framework resilient to the deformation process by modulating its own flexibility during the deformation process. Fig. 3f reports the unit cell volume changes upon tensile strain applied in the three directions at room temperature (see the corresponding profiles at 200 K and 0K in the Supplementary Figs. S24-S25, respectively). It is clear that when the tensile strain is applied along the [001] direction (before the strain-softening point), CALF-20 shows a very different unit cell volume expansion behavior than in the other directions. This is attributed primarily to the significant Negative Poisson Ratio (NPR) obtained during this process, the lowest value being of -0.35, as shown in Fig. 1c and Supplementary Fig. S12). Consequently, the constrain applies along the [001] direction and the structure expands along the *a*- and *b*-axis and then display auxetic behavior, as shown in Fig. 3g and Supplementary Fig. S26. When the tensile strain of the MOF along the [001] direction exceeds the strain-softening point, the phase transition occurs and the NPR feature disappears, showing non-axial behavior.

Reversible strain-induced phase transition mechanism. To further explore the structure deformation mechanism of CALF-20 under different strain loading, we defined three deformation angles by considering the Zn metal as the node of the

deformation framework and two different ligands as the rigid rods, as shown in Fig. 4a. Among them, ϕ and θ are defined as the angles of the lozenge lattice formed by triazolate grids, and ω represents the angle between the triazolate grids and oxalate ligands. As shown in Supplementary Fig. S27 and Figs. 4b-4c, the corresponding results indicate that all the angular changes of CALF-20 are linear before the critical strain regardless of the strained direction. This implies that the MOF is sufficiently robust to resist to mechanical deformation. It is particularly interesting to highlight that before and after the strain softening-point when the tensile strain is applied along the [001] direction, such deformation mechanism remains unchanged, suggesting that the CALF_20 structure presents a high flexibility in conjunction with a good mechanical strength. In particular, the linear relationship between the angular changes and the applied tensile strain is still preserved at >30% strain as shown in Fig. 4c and Supplementary Movie S1. This behavior is attractive for potential ultra-sensitive sensing applications.

To further elucidate the phase transition mechanism driven by the uniaxial tensile strain along the [001] direction, we conducted orbital Hamilton population (COHP) analysis,⁴⁵ which allows quantitative analysis of changes in interatomic couplings during stretching. As shown in Figs. 4d-4e, the broken symmetry in CALF-20 leads to independent changes in the chemical bonds between Zn atoms and its coordinated atoms. Fig. 4e evidences that the interactions between Zn and the oxalate ligands change only slightly in the whole strain range. Notably, the structural differences before/after the strain-softening point are mainly due to the different orientation of the oxalate ligands, as shown in Fig. 4d. The negative integrated COHP analysis revealed that the interactions between the single O or N atoms of the ligand and Zn metal change significantly before and after the phase transition, while the interactions between the overall Zn and the two ligands only slightly change, as shown in Figs. 4e-4f. This is because during the stretching process along [001] direction, the main deformation is the bending of the Zinc triazolate grid, and the oxalate ligand acts like a hinge during the deformation process. Therefore, CALF-20 is demonstrated to exhibit a distinct *two-*

step elastic deformation behavior when stretched along the [001] direction, as well as a switching from auxetic to non-auxetic behavior. This phenomenon is rarely reported in crystal,⁴⁶ indicating that CALF-20 may be promising in the fields of engineering materials, motion memory devices and strain sensors among others.^{47,48}

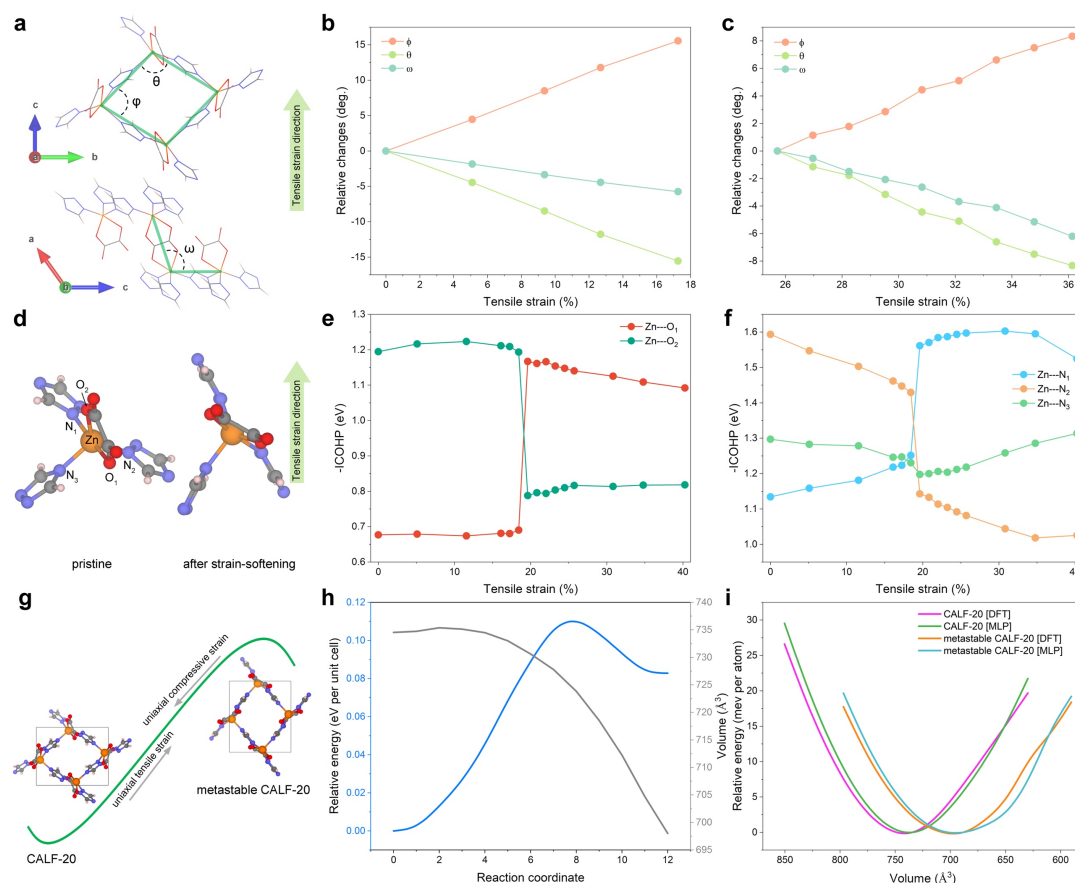


Fig. 4 | Strain-induced phase transition of CALF-20. (a) Scheme of CALF-20 along the *bc* (top) and *ac* (bottom) planes, where the angle ϕ and θ denote the angle between adjacent triazolate ligands in the lozenge lattice of CALF-20, and the angle ω represents the angle between the triazolate ligand and oxalate ligand. Relative angle changes (ϕ , θ , and ω) for the applied tension strain along the [001] direction (b) before strain-softening and (c) after strain-softening, respectively. (d) Typical CALF-20 structure component containing three 1,2,4-triazole and one oxalate functions. The five atoms coordinated to Zn metal are labelled (left: pristine CALF-20; right: CALF-20 after strain-softening). (e, f) Negative integrated crystal orbital Hamilton population ($-ICOHP$) values reported as a function of the strain applied along [001] direction for various Zn-coordinated atom pairs. The $-ICOHP$ values are scaled with the strength of the interactions. Color code: Zn, orange; N, blue; O,

red; C, grey; H, white. **(g)** Schematic illustration of the CALF-20 phase transition implying uniaxial tensile strain. **(h)** Energy landscape of the phase transition between the pristine structure and a metastable phase identified by generalized solid-state nudged elastic band (SS-NEB) approach.⁴⁹ Change of unit cell volume (\AA^3) relative is given by black lines. **(i)** Unit-cell volume vs energy plot for pristine structure and metastable phase from DFT and MLP-MD simulations, respectively.

The strained crystal structure is inherently unstable at ambient pressure. We therefore considered the structure after the strain-softening point and re-optimized it at the DFT level. Interestingly, it was found that the total energy of such configuration at 0K is only 83 meV unit-cell⁻¹ slightly higher than that of the pristine structure. Therefore, this new phase (termed as metastable CALF-20) is rearranged by applying uniaxial strain, showing strain-induced reversible phase transition behavior, as shown in Fig. 4g. These calculations indicate that the energy barrier for the phase transition from pristine to metastable CALF-20 is only 0.11 eV unit-cell⁻¹, whereas for the reverse phase transition the energy barrier is even lower (0.03 eV unit-cell⁻¹) (Fig. 4h and Supplementary Movie S2). This suggests that the newly identified structure is indeed a metastable phase that can readily switch towards the pristine structure by overcoming a very low energy barrier.

Discussions

In conclusion, high-accuracy DFT and MLP-MD simulations enabled to systematically explore the flexible behavior of CALF-20. This MOF was demonstrated to exhibit a coexistence of multiple negative phenomena simultaneously, including NAC, negative Poisson's ratio, and NTE, resulting in a unique dynamic response of the structure upon temperature and pressure stimuli. From a methodology standpoint, the development of an accurate MLP for the MOF framework was proved to be a key strategy to predict the mechanical properties at finite temperature with comparable numerical accuracy to DFT calculations and a much lower computational cost. Decisively CALF-20 was shown to possess a very unique strain-softening behavior along the [001] direction with

two nearly linear strain-stress curves under the ideal tensile strain applied, demonstrating an uncommon elastic deformation during the whole extension process. Importantly, the fracture strain of CALF-20 was determined to be 27% along the [001] direction at room temperature, a magnitude nearly twofold greater than the hitherto reported value for a MOF, specifically 14% in the case of Ni-TCPP⁴¹). This highlights that this material is very promising for biomechanical systems, flexible electronics and nanomechanical devices. Finally, the deformation of CALF-20 along the [001] direction was demonstrated to induce a newly metastable phase owing to its unique anisotropic flexibility. This observation is reminiscent to the phase β -CALF-20 very recently reported upon exposure of this MOF to humid environments.⁵⁰ Notably, the structural parameters of our computed metastable phase are in excellent agreement with the experimental parameters of β -CALF-20,⁵⁰ as show in Fig. 4g and Supplementary Table S4. In this respect, the developed MLP enabled to predict the energy landscape of this metastable phase accurately, as shown in Fig. 4i. Particularly considering the fact that such metastable phase has not been incorporated in the initial data set and MLP training, this suggests that the developed MLP can serve as a general-purpose potential to expand the computational exploration of CALF-20 towards new avenues.

Methods

DFT calculations

All DFT calculations were carried out using the Vienna *Ab-initio* Simulation Package (VASP) code (Version: 5.4.4).²⁴ The projector augmented wave (PAW) potential and the Perdew-Burke-Ernzerhof (PBE) exchange-correlation functional was adopted.^{51,52} An energy cutoff of 650 eV and a Monkhorst-Pack $3 \times 4 \times 3$ k-point grid⁵³ was chosen to ensure convergence of total energy and forces below 10^{-5} eV and 10^{-3} eV/Å, respectively. We also used the DFT-D3 Van der Waals (vdW) correction⁵⁴. The computed lattice parameters of the pristine CALF-20 were found in good agreement with the experimental values (Supplementary Table S5).

Dataset preparation

In order to obtain the training data for the MLPs introduced in this study, finite-temperature *ab-initio* molecular dynamics (AIMD) simulations were performed using the VASP code. These simulations involved $> 30,000$ snapshots within a $2 \times 2 \times 2$ supercell of CALF-20, using a time step of 0.5 fs. Brillouin zone sampling was performed using a Monkhorst-Pack k -point grid⁵³ of size $1 \times 1 \times 1$. All AIMD simulations adhered to the NVT ensemble framework, incorporating the Nosé-Hoover thermostat⁵⁵ to maintain a constant temperature of 100 ~800 K.

MLP development

To construct the MLP for CALF-20, the DeePMD-kit code (version 2.0.1)⁵⁶ was employed with the DeepPot-SE model.^{56,57} The size of the embedding network was set to $\{25, 50, 100\}$, while the fitting section consisted of $\{240, 240, 240\}$. Both networks utilize the ResNet architecture. ResNet architecture is utilized in both networks.⁵⁸ During the training process, a cutoff distance of 7.9 Å was applied, and a smoothing value of 2.1 Å was used. To ensure model robustness, the training and test data were allocated in a 3:1 ratio, effectively mitigating the risk of overfitting.

MLP-MD simulations

The MLP derived from the DFT was implemented in the following MLP-MD simulations through integration with the DeepMD-kit interface coupled with the LAMMPS code.^{56,59} In the MLP-MD simulations, the trained model served as a pair style within the LAMMPS framework, enabling the computation of both energy and force profiles during the MD simulations. The phonon dispersion spectra were calculated under strict convergence criteria with the Phonopy code, by using Lammmps as the calculator.^{30,59}

Classical MD simulations

MD simulations employing classical force fields were executed using the Lammmps code.⁵⁹ CALF-20 was treated as fully flexible with the potential parameters and 12-6 Lennard-Jones (LJ) site contributions from the universal force field (UFF).⁶⁰ The computation of 12-6 LJ parameters involved the application of Lorentz-Berthelot mixing rules.⁶¹ The distance cutoff for LJ interactions was set as 12 Å. Electrostatic interactions were determined using the Ewald summation method,⁶² with a tolerance

level of 10^{-6} . Atomic charges were determined utilizing the DDEC6 method.⁶³ To accommodate the simulation, a supercell with dimensions of $3 \times 3 \times 3$ was employed, thereby ensuring that the box size was twice the cutoff radius.

More detailed methodologies are provided in the *Supplementary Information*.

Data availability

All data needed to evaluate the conclusions in the paper are present in the paper and/or the Supplementary Information. The data related to this article can be accessed online at https://github.com/agrh/Data_Repository_CALF-20.

Code availability

The primary packages utilized in this article including VASP (<https://www.vasp.at>),²⁴ DeePMD-kit (<https://github.com/deepmodeling/deepmd-kit>),⁵⁶ and Lammmps (<https://www.lammps.org>).⁵⁹ Detailed information about the license and the user manual can be found in the abovementioned articles and on their websites.

References

1. Meng, W. *et al.* An elastic metal–organic crystal with a densely catenated backbone. *Nature* **598**, 298–303 (2021).
2. Howarth, A. J. *et al.* Chemical, thermal and mechanical stabilities of metal–organic frameworks. *Nat Rev Mater* **1**, 15018 (2016).
3. Burtch, N. C., Heinen, J., Bennett, T. D., Dubbeldam, D. & Allendorf, M. D. Mechanical Properties in Metal–Organic Frameworks: Emerging Opportunities and Challenges for Device Functionality and Technological Applications. *Adv. Mater.* **30**, 1704124 (2018).
4. Son, F. A. *et al.* Investigating the mechanical stability of flexible metal–organic frameworks. *Commun Chem* **6**, 185 (2023).

5. Wang, L., Luo, H., Deng, S., Sun, Y. & Wang, C. Uniaxial Negative Thermal Expansion, Negative Linear Compressibility, and Negative Poisson's Ratio Induced by Specific Topology in $\text{Zn}[\text{Au}(\text{CN})_2]_2$. *Inorg. Chem.* **56**, 15101–15109 (2017).
6. Shi, N., Song, Y., Xing, X. & Chen, J. Negative thermal expansion in framework structure materials. *Coordination Chemistry Reviews* **449**, 214204 (2021).
7. Nicolaou, Z. G. & Motter, A. E. Mechanical metamaterials with negative compressibility transitions. *Nature Mater* **11**, 608–613 (2012).
8. Baughman, R. H., Stafström, S., Cui, C. & Dantas, S. O. Materials with Negative Compressibilities in One or More Dimensions. *Science* **279**, 1522–1524 (1998).
9. Frenzel, T., Kadic, M. & Wegener, M. Three-dimensional mechanical metamaterials with a twist. *Science* **358**, 1072–1074 (2017).
10. Sun, M.-E. *et al.* Chirality-Dependent Structural Transformation in Chiral 2D Perovskites under High Pressure. *J. Am. Chem. Soc.* **145**, 8908–8916 (2023).
11. Cairns, A. B., Thompson, A. L., Tucker, M. G., Haines, J. & Goodwin, A. L. Rational Design of Materials with Extreme Negative Compressibility: Selective Soft-Mode Frustration in $\text{KMn}[\text{Ag}(\text{CN})_2]_3$. *J. Am. Chem. Soc.* **134**, 4454–4456 (2012).
12. Lin, J.-B. *et al.* A scalable metal-organic framework as a durable physisorbent for carbon dioxide capture. *Science* **374**, 1464–1469 (2021).

13. Nguyen, T. T. T., Lin, J.-B., Shimizu, G. K. H. & Rajendran, A. Separation of CO₂ and N₂ on a hydrophobic metal organic framework CALF-20. *Chemical Engineering Journal* **442**, 136263 (2022).
14. Nguyen, T. T. T., Shimizu, G. K. H. & Rajendran, A. CO₂/N₂ separation by vacuum swing adsorption using a metal–organic framework, CALF-20: Multi-objective optimization and experimental validation. *Chemical Engineering Journal* **452**, 139550 (2023).
15. Roy, S. *et al.* Functional wood for carbon dioxide capture. *Cell Reports Physical Science* **4**, 101269 (2023).
16. Singh, P., Singh, H. D., Menon, A. H. & Vaidhyanathan, R. Preferential CO₂ adsorption by an ultra-microporous zinc-aminotriazolato-acetate MOF. *Chem. Commun.* **59**, 5559–5562 (2023).
17. Naskar, S., Fan, D., Ghoufi, A. & Maurin, G. Microscopic insight into the shaping of MOFs and its impact on CO₂ capture performance. *Chemical Science* **14**, 10435–10445 (2023).
18. Goetjen, T. A. *et al.* Metal–organic framework (MOF) materials as polymerization catalysts: a review and recent advances. *Chem. Commun.* **56**, 10409–10418 (2020).
19. Behera, P., Subudhi, S., Tripathy, S. P. & Parida, K. MOF derived nano-materials: A recent progress in strategic fabrication, characterization and mechanistic insight towards divergent photocatalytic applications. *Coordination Chemistry Reviews* **456**, 214392 (2022).

20. Frenkel, D. & Smit, B. *Understanding molecular simulation: from algorithms to applications*. (Elsevier, 2023). doi:10.1016/B978-0-12-267351-1.X5000-7.
21. Demir, H., Daglar, H., Gulbalkan, H. C., Aksu, G. O. & Keskin, S. Recent advances in computational modeling of MOFs: From molecular simulations to machine learning. *Coordination Chemistry Reviews* **484**, 215112 (2023).
22. Boyd, P. G. *et al.* Data-driven design of metal–organic frameworks for wet flue gas CO₂ capture. *Nature* **576**, 253–256 (2019).
23. Lazzeri, M., Attaccalite, C., Wirtz, L. & Mauri, F. Impact of the electron-electron correlation on phonon dispersion: Failure of LDA and GGA DFT functionals in graphene and graphite. *Phys. Rev. B* **78**, 081406 (2008).
24. Kresse, G. & Furthmüller, J. Efficient iterative schemes for *ab initio* total-energy calculations using a plane-wave basis set. *Phys. Rev. B* **54**, 11169–11186 (1996).
25. Goodwin, A. L., Keen, D. A. & Tucker, M. G. Large negative linear compressibility of Ag₃ [Co(CN)₆]. *Proc. Natl. Acad. Sci. U.S.A.* **105**, 18708–18713 (2008).
26. Cliffe, M. J. & Goodwin, A. L. *PASCal*: a principal axis strain calculator for thermal expansion and compressibility determination. *J Appl Crystallogr* **45**, 1321–1329 (2012).
27. Cai, W. & Katrusiak, A. Giant negative linear compression positively coupled to massive thermal expansion in a metal–organic framework. *Nat Commun* **5**, 4337 (2014).

28. Serra-Crespo, P. *et al.* Experimental evidence of negative linear compressibility in the MIL-53 metal–organic framework family. *CrystEngComm* **17**, 276–280 (2015).
29. Martin, D. *Introduction to lattice dynamics*. (Cambridge university press, 1993).
30. Togo, A. & Tanaka, I. First principles phonon calculations in materials science. *Scripta Materialia* **108**, 1–5 (2015).
31. Zhou, W., Wu, H., Yildirim, T., Simpson, J. R. & Walker, A. R. H. Origin of the exceptional negative thermal expansion in metal-organic framework-5 Zn₄O(1,4-benzenedicarboxylate)₃. *Phys. Rev. B* **78**, 054114 (2008).
32. Shaidu, Y., Smith, A., Taw, E. & Neaton, J. B. Carbon Capture Phenomena in Metal-Organic Frameworks with Neural Network Potentials. *PRX Energy* **2**, 023005 (2023).
33. Monacelli, L., Errea, I., Calandra, M. & Mauri, F. Pressure and stress tensor of complex anharmonic crystals within the stochastic self-consistent harmonic approximation. *Phys. Rev. B* **98**, 024106 (2018).
34. Evans, J. D., Dürholt, J. P., Kaskel, S. & Schmid, R. Assessing negative thermal expansion in mesoporous metal–organic frameworks by molecular simulation. *J. Mater. Chem. A* **7**, 24019–24026 (2019).
35. Ogborn, J. M., Collings, I. E., Moggach, S. A., Thompson, A. L. & Goodwin, A. L. Supramolecular mechanics in a metal–organic framework. *Chem. Sci.* **3**, 3011 (2012).

36. Garai, B. *et al.* Reversible switching between positive and negative thermal expansion in a metal–organic framework DUT-49. *J. Mater. Chem. A* **8**, 20420–20428 (2020).
37. Burmistrov, I. S., Kachorovskii, V. Yu., Klug, M. J. & Schmalian, J. Emergent Continuous Symmetry in Anisotropic Flexible Two-Dimensional Materials. *Phys. Rev. Lett.* **128**, 096101 (2022).
38. Qin, G. & Qin, Z. Negative Poisson’s ratio in two-dimensional honeycomb structures. *npj Comput Mater* **6**, 51 (2020).
39. Jiang, C. & Srinivasan, S. G. Unexpected strain-stiffening in crystalline solids. *Nature* **496**, 339–342 (2013).
40. Jaspers, M. *et al.* Ultra-responsive soft matter from strain-stiffening hydrogels. *Nat Commun* **5**, 5808 (2014).
41. Cheng, J. *et al.* Achieving Superior Tensile Performance in Individual Metal–Organic Framework Crystals. *Advanced Materials* 2210829 (2023) doi:10.1002/adma.202210829.
42. Tricarico, M., Besnard, C., Cinque, G., Korsunsky, A. M. & Tan, J.-C. Stress–strain relationships and yielding of metal-organic framework monoliths. *Commun Mater* **4**, 86 (2023).
43. Widmer, R. N., Bumstead, A. M., Jain, M., Bennett, T. D. & Michler, J. Plasticity of Metal–Organic Framework Glasses. *J. Am. Chem. Soc.* **143**, 20717–20724 (2021).

44. Wei, Y., Ashling, C. W., Watcharatpong, T., Fan, Z. & Horike, S. Hierarchical Metal-Organic Network-Forming Glasses toward Applications. *Adv Funct Materials* 2307226 (2023) doi:10.1002/adfm.202307226.
45. Maintz, S., Deringer, V. L., Tchougréeff, A. L. & Dronskowski, R. LOBSTER: A tool to extract chemical bonding from plane-wave based DFT: Tool to Extract Chemical Bonding. *J. Comput. Chem.* **37**, 1030–1035 (2016).
46. Kulkarni, A. J., Zhou, M., Sarasamak, K. & Limpijumngong, S. Novel Phase Transformation in ZnO Nanowires under Tensile Loading. *Phys. Rev. Lett.* **97**, 105502 (2006).
47. Liu, Y. *et al.* Stretchable Motion Memory Devices Based on Mechanical Hybrid Materials. *Advanced Materials* **29**, 1701780 (2017).
48. Amjadi, M., Kyung, K.-U., Park, I. & Sitti, M. Stretchable, Skin-Mountable, and Wearable Strain Sensors and Their Potential Applications: A Review. *Adv. Funct. Mater.* **26**, 1678–1698 (2016).
49. Henkelman, G., Uberuaga, B. P. & Jónsson, H. A climbing image nudged elastic band method for finding saddle points and minimum energy paths. *The Journal of Chemical Physics* **113**, 9901–9904 (2000).
50. Chen, Z. *et al.* Humidity-Responsive Polymorphism in CALF-20: A Resilient MOF Physisorbent for CO₂ Capture. *ACS Materials Lett.* 2942–2947 (2023) doi:10.1021/acsmaterialslett.3c00930.
51. Blöchl, P. E. Projector augmented-wave method. *Phys. Rev. B* **50**, 17953–17979 (1994).

52. Perdew, J. P., Burke, K. & Ernzerhof, M. Generalized Gradient Approximation Made Simple. *Phys. Rev. Lett.* **77**, 3865–3868 (1996).
53. Monkhorst, H. J. & Pack, J. D. Special points for Brillouin-zone integrations. *Phys. Rev. B* **13**, 5188–5192 (1976).
54. Grimme, S. Semiempirical GGA-type density functional constructed with a long-range dispersion correction. *J. Comput. Chem.* **27**, 1787–1799 (2006).
55. Nosé, S. A unified formulation of the constant temperature molecular dynamics methods. *The Journal of Chemical Physics* **81**, 511–519 (1984).
56. Wang, H., Zhang, L., Han, J. & E, W. DeePMD-kit: A deep learning package for many-body potential energy representation and molecular dynamics. *Computer Physics Communications* **228**, 178–184 (2018).
57. Zhang, L., Han, J., Wang, H., Car, R. & E, W. Deep Potential Molecular Dynamics: A Scalable Model with the Accuracy of Quantum Mechanics. *Phys. Rev. Lett.* **120**, 143001 (2018).
58. He, K., Zhang, X., Ren, S. & Sun, J. Deep Residual Learning for Image Recognition. *Proceedings of the IEEE Conference on Computer Vision and Pattern Recognition (CVPR)* 770–778 (2016).
59. Thompson, A. P. *et al.* LAMMPS - a flexible simulation tool for particle-based materials modeling at the atomic, meso, and continuum scales. *Computer Physics Communications* **271**, 108171 (2022).

60. Rappe, A. K., Casewit, C. J., Colwell, K. S., Goddard, W. A. & Skiff, W. M. UFF, a full periodic table force field for molecular mechanics and molecular dynamics simulations. *J. Am. Chem. Soc.* **114**, 10024–10035 (1992).
61. Lorentz, H. A. Ueber die Anwendung des Satzes vom Virial in der kinetischen Theorie der Gase. *Annalen der physik* **248**, 127–136 (1881).
62. Essmann, U. *et al.* A smooth particle mesh Ewald method. *The Journal of Chemical Physics* **103**, 8577–8593 (1995).
63. Manz, T. A. & Limas, N. G. Introducing DDEC6 atomic population analysis: part 1. Charge partitioning theory and methodology. *RSC Adv.* **6**, 47771–47801 (2016).

Acknowledgments

The computational work was performed using HPC resources from GENCI-CINES (Grant A0140907613).

Author contributions

D.F. and G.M. designed the research. D.F. and S.N. carried out the simulations. D.F., S.N., and G.M. wrote the manuscript. G.M. supervised the research.

Competing interests

The authors declare that they have no competing interests.

Additional information

Supplementary information

The online version contains supplementary material available at